Radio Science

RESEARCH ARTICLE
10.1029/2018RS006701

Demonstrating the Use of a Class of Min-Max Smoothers for *D* Region Event Detection in Narrow Band VLF Phase

S. I. Lotz[1] **and M. Clilverd**[2]

[1]SANSA Space Science, Hermanus, South Africa, [2]British Antarctic Survey, Cambridge, United Kingdom

Key Points:
- We demonstrate the use of LULU operators for event detection in narrow band VLF signal phase
- LULU is used to identify solar flares, EMIC wave precipitation events, and substorms from VLF phase
- We show that events could be isolated without the explicit need for estimating a quiet day curve

Correspondence to:
S. I. Lotz,
slotz@sansa.org.za

Citation:
Lotz, S. I., & Clilverd, M. A. (2019). Demonstrating the use of a class of min-max smoothers for *D* region event detection in narrow band VLF phase. *Radio Science*, *54*, 233–244. https://doi.org/10.1029/2018RS006701

Received 7 AUG 2018
Accepted 12 FEB 2019
Accepted article online 17 FEB 2019
Published online 5 MAR 2019

Abstract This paper describes the use of a class of nonlinear smoothers for the identification of interesting phenomena in narrow band very low frequency (VLF) transmission phase caused by perturbation events in the *D* region of the ionosphere. The LULU smoothers, named for their smoothing of upward (L) and downward (U) peaks in a signal, usually used for image processing tasks, are described, and examples are shown where these operators are used to automatically isolate and identify features in the phase of narrow band transmissions received at high and high-middle latitudes (Antarctica and Marion Island, respectively). Identification of solar flare events, electromagnetic ion cyclotron wave precipitation, and substorm injection events are demonstrated, showing the potential for this technique to be used for space weather monitoring.

1. Introduction

Very low frequency (VLF) waves propagating subionospherically in the Earth-ionosphere waveguide respond to changing ionospheric conditions by changes in phase and amplitude. Therefore, observed perturbations to the otherwise constant carrier-phase of man-made VLF transmissions are routinely used as a sounding device of the bottom-side ionosphere (e.g., Clilverd et al., 2017). Characteristic changes in the number and energy density of charged electrons in the *D* region ionosphere (approximately 50–90 km altitude) signify the occurrence of events such as precipitation of electrons from the radiation belts due to wave-particle interactions (e.g., Rodger et al., 2008), increased ionization due to high X-ray flux following solar flares (e.g., Thomson et al., 2005), and electron precipitation during substorm injection events (Clilverd et al., 2008).

VLF receivers such as those operated by the AARDDVARK network (Clilverd et al., 2009) receive transmissions from powerful transmitters, placed mostly in the Northern Hemisphere, at various fixed frequencies. Transmitted signals are stable in frequency and phase, with mostly constant power output, and propagate long distances within the Earth-ionosphere waveguide, making these signals ideal for sounding the bottom-side ionosphere (e.g., Rodger et al., 2012; Thomson et al., 2005).

The aim of this work is to illustrate the use of a class of nonlinear smoothers to highlight features in narrowband VLF signal phase that are of interest to the VLF and broader space physics community. These "LULU" operators are a class of minimum-maximum smoothers designed by Rohwer (2005) that are mostly used in image processing applications (e.g., Anguelov & Fabris-Rotelli, 2008; 2010; Jankowitz, 2007). To the best of our knowledge, these operators have not been used in geophysics applications before. A number of characteristics of the LULU operators make them attractive for event identification in VLF phase data:

1. They are strictly variation reducing, meaning spurious elements are not added in the smoothing process (Rohwer, 2005).
2. The *L* and *U* operators, defined in section 3, allows positive and negative block pulses (i.e., upward or downward peaks) in data to be identified separately (Rohwer, 2005).
3. Block pulses are identified only by their width (i.e., duration in a time series), allowing identification of events based on their typical duration regardless of amplitude.

In this study we utilize narrow band VLF transmission signals received at the South African National Antarctic Expedition IV (SANAE IV) base and at the South African base on Marion Island (Figure 1). SANAE IV is at L-shell of approximately 4.5, just outside of the typical plasmapause position (Carpenter, 1963). Marion Island is at $L \approx 2.3$—its middle-latitude location isolating it from the common occurrence of high-latitude

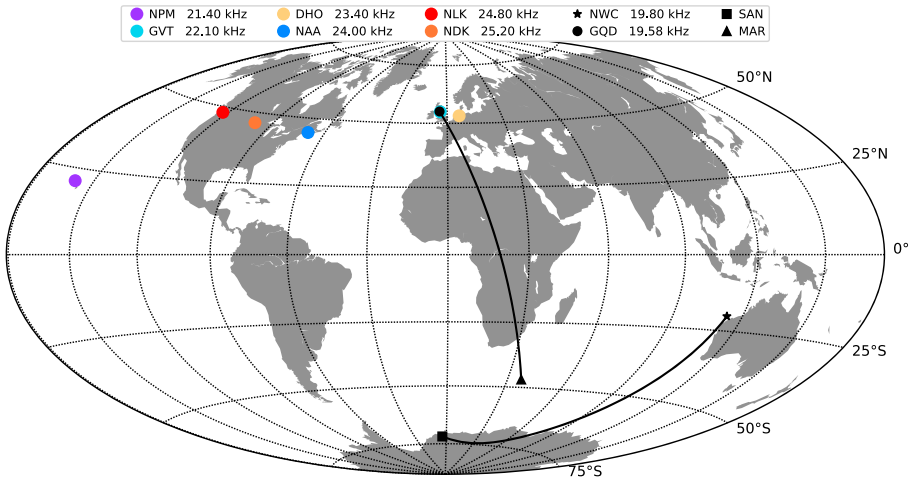

Figure 1. Locations of high power transmitters that are received at Marion Island (MAR) and South African National Antarctic Expedition IV (SAN). The great circle propagation paths of the two transmissions utilized in this study are indicated with black curves.

phenomena such as energetic particle precipitation (Wenzel et al., 2016). Three-letter station codes SAN and MAR are used throughout the rest of the paper for SANAE IV and Marion Island, respectively. Geographic coordinates of SAN is (71.667°S, 2.833°W), and MAR is at (46.867°S, 37.867°E).

The paper is laid out as follows: The data sets of VLF signals received at SAN and MAR are briefly described in the next section, while the LULU operators and some of their important properties are discussed in section 3. In section 4 the application of these operators to several events is demonstrated, and the paper is summarized in the last section.

2. Data Sets and Instruments Utilized

Apart from broadband VLF signal, the antennas at Marion Island and SANAE receive transmissions from a number of Northern Hemisphere transmitters and one in the Southern Hemisphere located at North-West Cape in Australia (station code NWC). The narrow band transmissions come from large, powerful naval transmitters that operate at well-defined frequencies, near-continuously, and with high phase stability most of the time.

Broadband VLF signal is received by orthogonal loop antennas pointing northward and eastward, respectively. Received signal is sampled with computer audio cards and processed by the UltraMSK software-defined radio system (see www.ultramsk.com). Narrow band components of the broadband signal, corresponding to the relevant transmitters, are processed by implementations of the UltraMSK software to yield phase and amplitude data at 1-s intervals for each transmitter.

Only transmissions from GQD in Britain (at 19.58 kHz) to MAR and NWC (19.80 kHz) to SAN are analyzed in this work. Data from these adequately illustrate the use of the LULU operators in VLF-related research. The map in Figure 1 shows the location of transmitters received at MAR and SAN, with the GQD-MAR and NWC-SAN great circle propagation paths indicated.

The signals propagate within the Earth-ionosphere waveguide, with low attenuation, such that they are detectable over long distances. Excess ionization generated in the upper waveguide boundary (the *D* region), due to processes such as solar flares, changes the signal propagation conditions along the great circle path between transmitter (Tx) and receiver (Rx) and causes phase and amplitude perturbations to the received signal.

Subionospheric propagation paths from European transmitters to MAR and SAN experience very little longitudinal variation. Such great circle paths are good for monitoring solar flares since total daylight illumination time is maximized. It is generally good to avoid paths that cross the day-night terminator, as this causes a complicated phase curve, making the identification of specific phenomena difficult, although large flares can still be identified on paths that are not fully illuminated (e.g., Thomson et al., 2005). Transmissions from

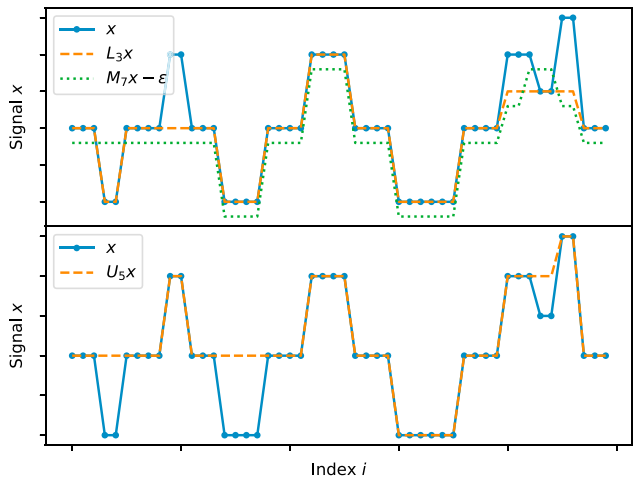

Figure 2. Demonstration of LULU operators L_n, U_n, and the median filter M_n. Signal x consists of negative and positive blockpulses of widths 2, 3, 4, and 6 imposed on the zero sequence. Operators L_3 and U_5 are applied to x, annihilating upward pulses up to width 3 and downward pulses up to width 5. In its comparison with L_3 we see the median filter introduces a spurious peak when smoothing the double peak on the right. Note that M_kx is offset with $-\epsilon$ for clarity.

Australia (NWC at 23.40 kHz) to SAN pass under the footprints of the radiation belts, and this is good for monitoring precipitation from radiation belt processes.

In section 4.1 we utilize data from the GOES spacecraft to analyze flare-induced X-ray flux for a number of events during September 2017. Data were accessed through the National Geophysical Data Center data archive (https://www.ngdc.noaa.gov/stp/satellite/goes/index.html).

In sections 4.2 and 4.3 geomagnetic field data at Halley base in Antarctica (geographic coordinates 75.6°S, 26.18°W) is utilized to analyze electromagnetic ion cyclotron (EMIC) waves and substorms in the X-component geomagnetic field. This is measured by a search coil magnetometer (SCM) delivering data at 0.1-s cadence. Data from this instrument are available from the British Antarctic Survey data service (http://psddb.nerc-bas.ac.uk/).

3. LULU Operators

Rohwer (2005) introduced LULU operators as a class of nonlinear smoothers in the same vein as median smoothers, but constructed by minimum and maximum selectors. Their characteristics make them especially attractive for image processing applications (e.g., Anguelov & Fabris-Rotelli, 2010) and impulsive noise removal and enable a framework for multiresolution analysis (Rohwer, 2005).

This section is dedicated to summarizing the relevant operators and discussing the properties that make them attractive to the analysis of VLF time series data.

3.1. Operator Definitions

Consider the selectors $\min_n$ and $\max_n$ that take the minimum and maximum over a window of width n of the finite sequence $x = \{x_i\}, i = 1, 2, \ldots, N$:

$$\min_n x_i = \min\{x_i, x_{i+1}, \ldots, x_{i+n}\}, \tag{1}$$

$$\max_n x_i = \max\{x_i, x_{i+1}, \ldots, x_{i+n}\}. \tag{2}$$

The $\max_n$ ($\min_n$) operator defines the upper (lower) envelope of x with window-size n. Related to the n-envelope is the concept of an upward or downward "blockpulse" of a certain width. Signal x contains an upward (or positive) blockpulse of length n if $x_i < x_{i+1} = x_{i+2} = \ldots = x_{i+n} > x_{i+n+1}$, for some $i \in \{1, \ldots, N - n - 1\}$. The amplitude of the block pulse is $x_j - \max\{x_i, x_{i+n+1}\}$, with $i < j \leq i + n$. A downward or negative blockpulse is defined in a similar manner.

The combination of the operators (1) and (2) results in the more powerful operators L_n ("lower") and U_n ("upper"), also defined over the window n:

$$L_n = \max_n \min_n, \tag{3}$$

$$U_n = \min_n \max_n. \tag{4}$$

L_nx annihilates all upward blockpulses up to width n, preserving upward pulses of width $> n$ and downward blockpulses of any width. Similarly, U_n annihilates downward blockpulses of width $\leq n$ but preserves all upward pulses and all downward pulses of width $> n$. Figure 2 demonstrates L_3 and U_5 operating on a signal x consisting of positive and negative blockpulses of widths 2, 3, 4, and 6. In the top panel of Figure 2 all the upward pulses with width ≤ 3 are annihilated by L_3 while the rest of the signal is preserved perfectly. The double peak near the end of the signal is flattened to a wider peak of width 7. In the lower panel U_5x only eliminates the negative pulses of widths 2 and 4, but not the widest downward pulse, as its width is greater than 5. The double peak is interpreted as a single negative pulse of width 2 and is removed as expected.

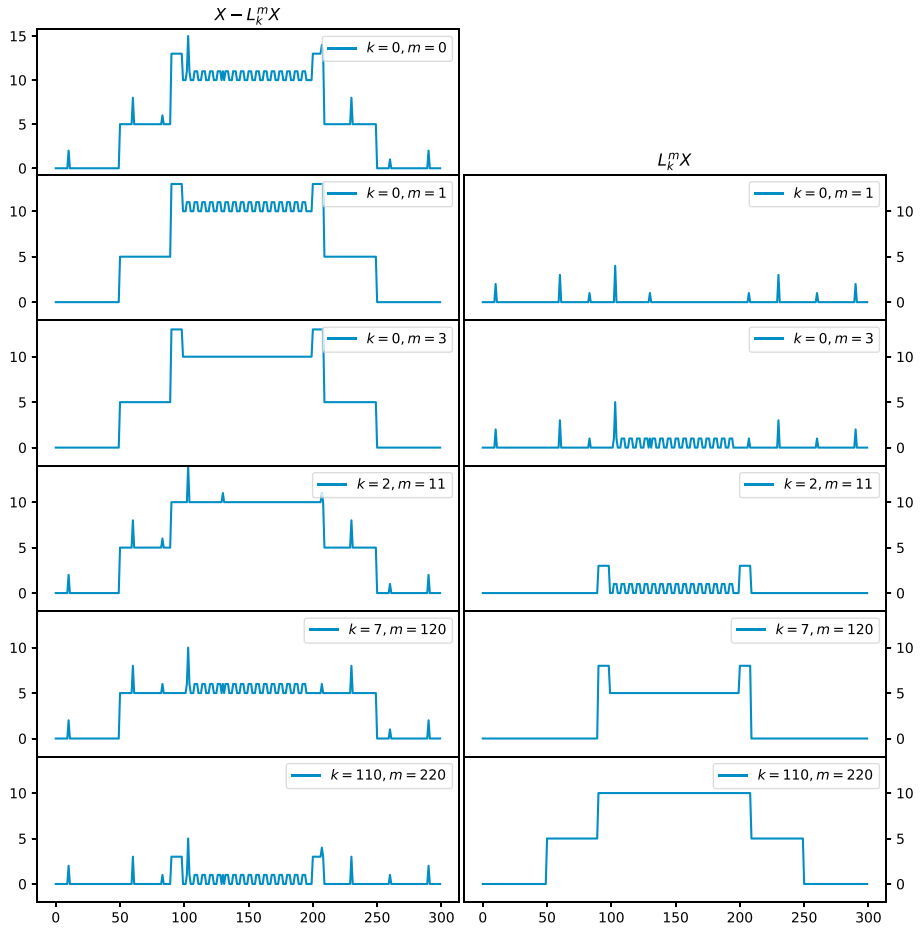

Figure 3. Noisy castle signal decomposed with the band-pass operator $L_k^m x$ (see equation (7)). Panels on the left show residual signal and the band-pass filtered signal on the right-hand side. In the second row, only the most narrow peaks (width 1) are removed. For the rest of the rows, resolution levels k and m are chosen so that two sets of constituent pulses are highlighted. Figure adapted from Rohwer (2005, chapter 9).

A simple illustration is used to compare L_n with the median filter M_k. In the top panel the dotted line indicates the median filter M_{2n+1} $(n = 3)$ applied to x and shifted by ϵ for clarity. The median filter accurately removes all pulses of width ≤ 3 but introduces a spurious pulse at the double peak. This indicates two important differences between M_k and L_n: The median filter does not enable easy distinction between positive and negative pulses, while this is natural for L_n (and U_n), and the median filter is not strictly variation reducing, causing spurious peaks to be introduced to the smoothed signal.

The "half-smoothers" L_n and U_n are combined to form full smoothers that remove positive and negative blockpulses. The floor (F_n) and ceiling (C_n) operators are defined by recursively applying L_n and U_n (Rohwer, 2005, chapter 4). The naming convention is suggestive of their respective definition: that F_n operates by eliminating upward pulses before downward pulses and C_n removes negative pulses before positive ones.

The L and U operators, and their compounds C_n and F_n, all exhibit fundamental features that enable the consistent decomposition of a signal into its constituent blockpulses. LULU operators are idempotent—meaning that repeated application of the same operator does not change the signal after the initial application, for example, $P(Px) = Px$ for arbitrary idempotent operator P. They are also coidempotent, meaning that the residual of the signal, $(I - P)x$, is invariant under repeated application, for example $(I - P)^2 x = (I - P)x$, with I the identity operator. The (i) idempotence and (ii) coidempotence of LULU operators are important, as they imply that there is (i) no noise left in the smoothed signal and that (ii) there is no signal left in the residual after smoothing.

Another valuable property of these operators is that they are variation reducing—always reducing the amount of variability of the input signal x or not affecting it at all (e.g., in case of repeated application)—but never adding spurious elements. Jankowitz (2007) provides a good, detailed illustration of these properties.

The consistency of signal decomposition by LULU operators enables a multiresolution analysis of a signal. The discrete pulse transform (DPT; Anguelov & Fabris-Rotelli, 2010; Rohwer, 2005, chapter 8) enables a decomposition of x in to constituent signals $D_n x$, representing resolution component "n" with block pulses of width n:

$$D_n = C_{n-1}x - C_n x, \quad n \geq 1. \tag{5}$$

The DPT can then be written as the series

$$D(x) = [D_1 x, D_2 x, \ \ldots, D_N x, D_0 x], \text{ with } \ D_0(x) = C_N(x). \tag{6}$$

We utilize the characteristics of the LULU operators and the DPT to define a type of band-pass filter to isolate upward pulses between width k and m:

$$L_k^m x = (L_k - L_m)x. \tag{7}$$

Figure 3 shows an example of how a noisy "castle" signal x, comprised of positive pulses of various widths (1, 2, 10, 119, and 199), may be decomposed using the L_k^m operator (figure adapted from Rohwer, 2005, chapter 9). The panels on the left show residual signal $x - L_k^m x$, and the filtered signal $L_k^m x$, with k and m increasing so that more than one set of constituent pulses are highlighted. This image serves to illustrate the ability of L_k^m to isolate upward pulses covering a band of widths and that no spurious elements are added when these components are filtered out, making clear the variation reducing properties of this operator.

4. Results: Examples of Events Isolated With LULU Operators

The effect of solar flares, EMIC wave precipitation, and substorm injection events are all clearly visible in the phase and, to a lesser extent, amplitude of subionospheric VLF transmissions. This section demonstrates the use of the LULU operators to identify various phenomena in VLF transmitter subionospheric phase curves. Identification in amplitude is possible, but not as clearly as with phase, and this is not shown.

4.1. Solar Flares

A recent spurt of solar activity resulted in a number of solar flares over 5 days (6–10 September 2017). These flares were observed at MAR and SAN on transmissions from European transmitters GQD, GVT, and DHO, among others (see Figure 1).

A typical flare signature in narrow band phase is a sharp increase over a few minutes, with a longer recovery during which the phase decreases to preflare level. Recovery from intense flares usually take up to a few hours (Thomson et al., 2005). To identify solar flares, we isolate the band of positive block pulses in the signal phase ϕ lasting between $k = 5$ and $m = 200$ min, using the filter L_k^m (equation (7)). The values of k and m are selected to smooth out high-frequency peaks (i.e., blockpulses narrower than k) and to remove slowly varying components of the signal (i.e., very wide blockpulses). In the case of flare detection we choose narrow cutoff to be 5 min, that is, $k = 5 \times 60 = 300$ s for signal ϕ measured at 1-s cadence and $m = 200$ min (3.3 hr or 12,000 s). In general, the choice of k and m is determined by the type of phenomena to be isolated and the signal noise characteristics. In this case $k = 5$ min is narrow enough to remove high-frequency noise, and $m = 200$ is wide enough to isolate the flares but narrow enough to not include the diurnal quiet day variation in phase.

Figure 4 shows phase ϕ (blue) of the GQD-MAR transmission for each day from 6–10 September 2017, with the filtered phase $z = L_k^m \phi$ (orange) and the residual $\phi - z$ (green). Multiple flares are observed on these days (first five panels of Figure 4). Day time on the path is defined as periods when the solar zenith angle is $\chi < 90°$ at the transmitter and the receiver. According to this definition the GQD-MAR path is day-lit for from approximately 0600 to 1500 UT for these dates. Vertical lines mark the start and end of "local" daytime. A typical quiet day phase curve from 19 July 2017 is displayed in the last panel of Figure 4. As the Earth is illuminated by the sun, the ionization in the ionosphere increases toward local noon time and hence the phase, decreasing toward dusk and night time.

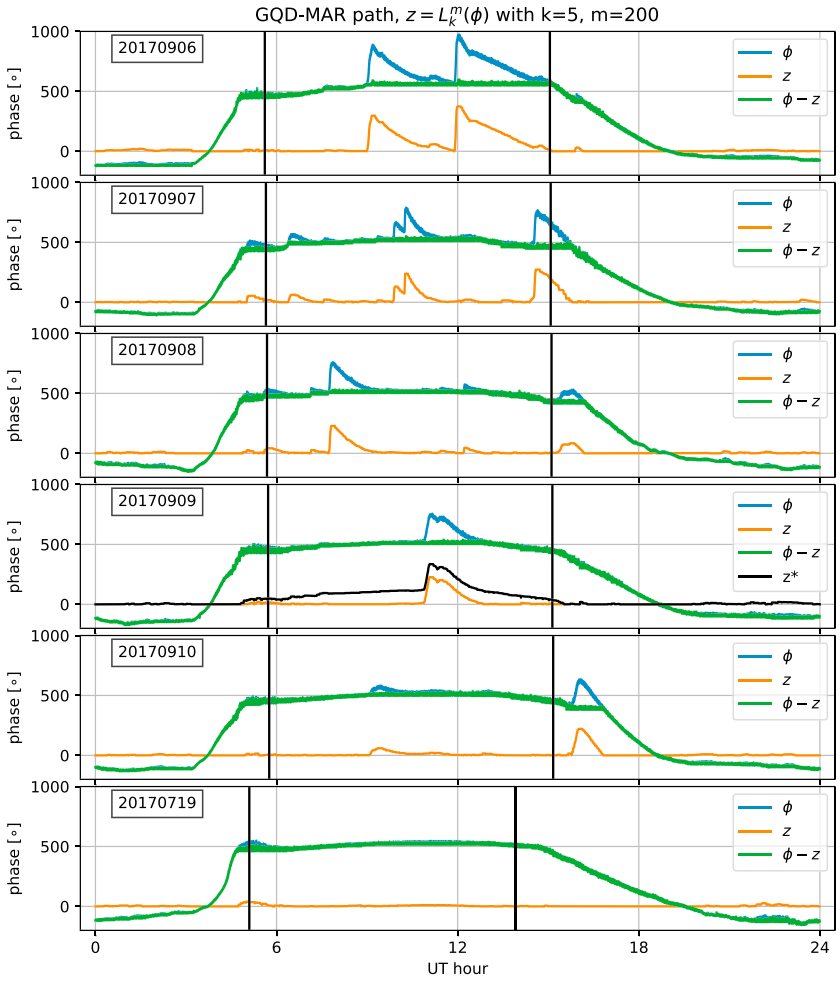

Figure 4. Band-pass discrete pulse transform $z = L_k^m\phi$ (equation (7)) applied to phase of the GQD-MAR transmission on a number of days when flares were observed (6–10 September 2017), as well as one quiet day (19 July 2017). In this example we set $k = 5$ and $m = 200$ min. Vertical black lines indicate sunrise and sunset in terms of χ computed at Tx and Rx locations. The black curve (z^*) on 19 July 2017 shows $L_k^m\phi$ with m chosen too high ($m = 650$ min), so that some residual quiet day variation is included.

The filtered signal z accurately captures every one of the major perturbations visible on top of the slowly varying quiet day curve. Some low amplitude artifacts are present in the z signal near the start and end of the day. These are due to midnight sector effects, for example, near 2 UT on 6 September 2017 and just before 24 UT on 7 September 2017.

The black curve labeled z^* in Figure 4 (panel 20170909) shows what happens if m is chosen to be too wide ($m = 650$ min). A portion of the diurnal variation is included in the identification of the flare-induced peak, resulting in a much longer duration than the actual event. Therefore, care must be taken to correctly identify the typical duration of the events under investigation. Nevertheless, the L_k^m operator provides a simple mechanism for identifying perturbation events without the complex task of specifying the nondisturbed VLF quiet-day-curve beforehand and the resulting data requirements. Usually, this task requires averaging of a large set of data to find the diurnal and annual variation in narrow band VLF signal (e.g., Cresswell-Moorcock et al., 2015).

On 6 September two M-class flares occurred shortly after each other, not allowing full recovery of the ionosphere in between events. In this case the L_k^m operator does not fully separate the events, as is evident by the near-constant residual $\phi - z$ of over 600°, while the quiet-day maximum phase is around 500° on this path (for this time of year). This could result in the under estimation of the intensity and duration of closely separated flares in a near-real time identification scheme based only on $L_k^m\phi$.

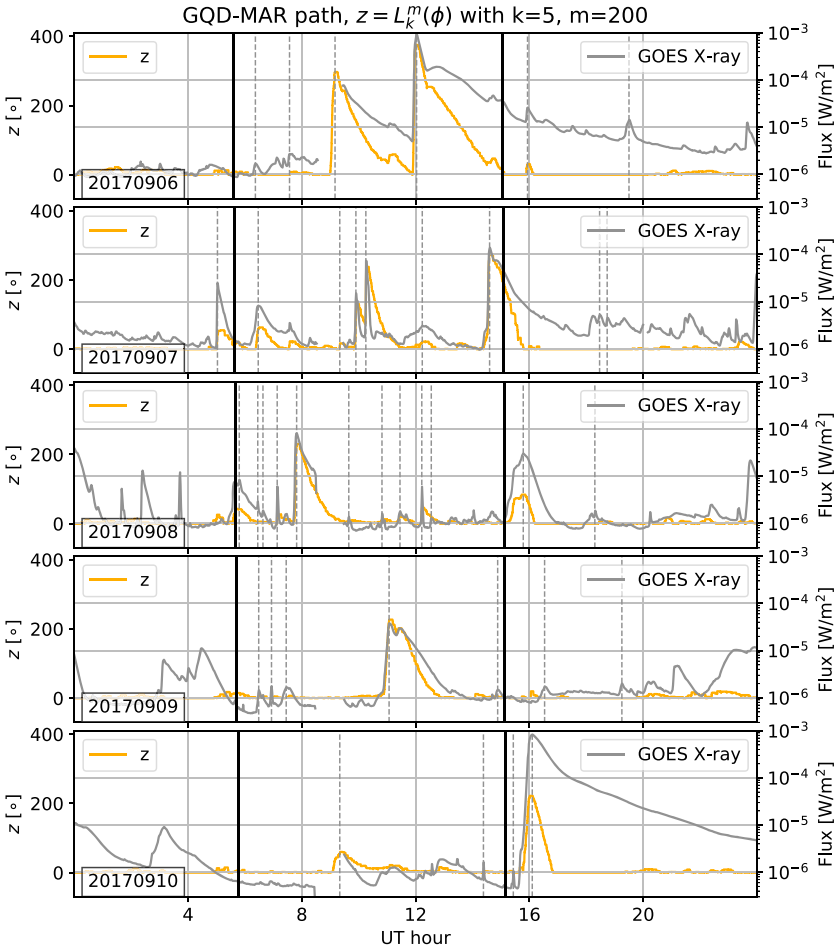

Figure 5. Filtered phase $z = L_k^m \phi$ (orange) with GOES X-ray flux (gray) for 6–10 September 2017. As in Figure 4 the vertical black lines indicate sunrise and sunset. Vertical dashed lines indicate flare peak times listed in Table 1.

In Figure 5 we compare z with equivalent X-ray flux observed in the 0.1- to 0.8-nm band aboard the GOES spacecraft observed in September 2017. Table 1 lists flares with their peak flux value occurring between 05:00 and 20:00 UT on 06–10 September 2017. The vertical dashed lines in Figure 5 indicate these peaks. These events lists are available online (ftp://ftp.swpc.noaa.gov/pub/indices/events/). The onset of the C, M, and X class flares are accurately highlighted in z. Regular outages in GOES data were experienced every day between about 08:30 and 09:30 UT.

As in Figure 4 black vertical lines indicate sunrise and sunset at the latest and earliest times for Tx and Rx pairs, respectively. It seems as if the gradual recovery from the flare-induced phase shift is cut short on 10 September by dusk, as the flare occurs after sunset and the GQD-MAR path is no longer illuminated by the flare X-ray fluxes. This is illustrated by the gradual decrease in X-ray flux versus the relatively abrupt recovery in phase after sunset. A similar discrepancy in recovery times is seen for the flare peaking at 09:10 on 6 September. This may simply be due to the ionosphere not having time to recover before the next flare impact.

In Figure 6 peak phase advance z is compared against the peak X-ray flux of flares and plotted for the 06–10 September events identified in Figure 4. The approximately logarithmic relationship between X-ray flux and phase advance described by Thomson et al. (2005) is observed here, although not perfectly. All flares causing $z > 40°$ (arbitrarily chosen threshold) peak phase change are plotted. Observations indicated with empty circles are the two flares observed after local sunset on 8 and 10 September. A logarithmic fit is applied to the reduced set of flares (solid line), which excludes the two "dusk-time" flares, yielding a fit of $R = 0.95$. Thomson et al. (2005) estimated maximum phase change (in μs) versus peak flux (in dBμW/m^2) with a

Table 1
Flare Events with Peak Flux between 05 and 20 UT Recorded by the GOES-13 and GOES-15 Spacecraft

Day (Sept 2017)	Peak time (UT)	Flare Class (–)	Flux (W/m^2)
06	06:22	C1.6	9.3e-04
06	07:34	C2.7	2.5e-03
06	09:10	X2.2	1.3e-01
06	12:02	X9.3	5.7e-01
06	15:56	M2.5	1.4e-02
06	19:30	M1.4	8.9e-03
07	05:02	M2.4	7.3e-03
07	06:28	C8.2	8.4e-03
07	09:20	C2.3	7.0e-04
07	09:54	M1.4	4.0e-03
07	10:15	M7.3	1.4e-02
07	12:14	C3.0	4.8e-03
07	14:36	X1.3	1.2e-01
07	18:28	C5.2	7.8e-03
07	18:44	C4.5	1.8e-03
08	05:48	C8.3	8.1e-03
08	06:27	C2.9	4.2e-04
08	06:38	C1.7	3.9e-04
08	07:08	C6.0	9.2e-04
08	07:49	M8.1	4.7e-02
08	09:39	C1.3	2.2e-04
08	10:49	C1.6	3.2e-04
08	11:27	C1.7	1.0e-03
08	12:13	C5.9	8.1e-04
08	12:33	C1.2	6.3e-04
08	15:47	M2.9	5.3e-02
08	18:18	C1.7	2.9e-04
09	06:29	C1.4	9.9E-04
09	06:56	C1.7	4.0E-04
09	07:27	C1.5	1.7E-03
09	11:04	M3.7	7.1E-02
09	14:53	C1.4	8.3E-04
09	16:32	C1.7	1.8E-03
09	19:15	C1.8	9.0E-04
10	09:20	C2.9	4.4e-03
10	14:23	C1.6	2.7e-04
10	15:26	C1.0	1.4e-04
10	16:06	X8.2	1.4e00

linear fit with gradient of about −2 on the propagation path NLK ($f_1 = 24.8$ kHz) to Dunedin, New Zealand (great circle distance $D_1 = 12.3$ Mm). A linear fit applied to z (converted to μs) on the GQD-MAR path ($D_2 = 11.9$ Mm) versus peak flux [dB$\mu W/m^2$] for the events in Figure 6 has a slope of approximately −1.56 (not shown). The difference could be explained by the shorter path length and lower frequency of the GQD-MAR transmission, compared to NLK-Dunedin: The NLK-Dunedin wavelength distance is $D_1/\lambda_1 = D_1 f_1/v = 12.3 \times 10^6 \cdot 24,800/v \approx 3.05 \times 10^{11}/v$ wavelengths. However, on the GQD-MAR path the distance is $D_2 f_2/v = 11.9 \times 10^6 \cdot 19,580/v \approx 2.33 \times 10^{11}/v$. Assuming the same speed v for each path, the wavelength ratio is

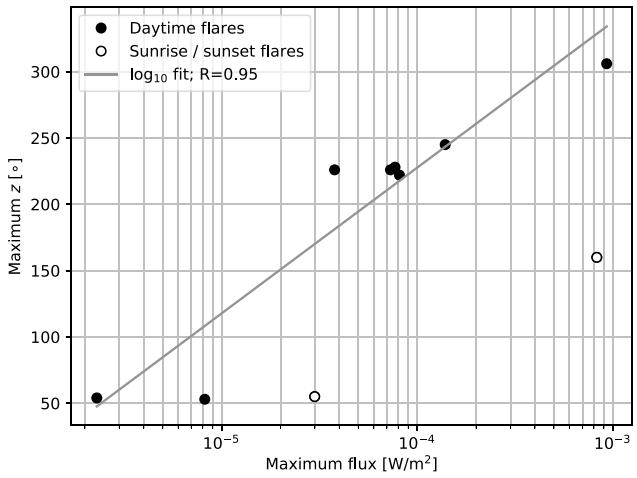

Figure 6. Logarithmic fits applied to the peak z calculated on GQD-MAR propagation path and peak flux observed in long wavelength X-ray flux aboard GOES. Empty circles indicate flares that are affected by sunrise and sunset conditions. The solid fit line is applied only to the selected set (filled circles). Fit quality is indicated in terms of correlation coefficient R.

around $2.33/3.05 = 0.76$. This is close to the ratio of observed flux to phase change ($-1.56/-2 = 0.78$) reported here and by Thomson et al. (2005).

4.2. EMIC Wave Precipitation

EMIC wave-induced precipitation of electrons in to the ionosphere acts as a loss mechanism for energetic electrons from the outer radiation belt (e.g., Clilverd et al., 2015). The precipitation of these electrons can affect VLF signals that propagate under appropriate L-shells, close to the footprints of the L-shells associated with the plasmapause (Rodger et al., 2008). A ground-based signature of EMIC waves that can induce precipitation is intervals of Pc1-2 (period 0.2–1 s, frequency 0.1–5 Hz) pulsations with diminishing period (IPDP; Hendry et al., 2016). EMIC wave-induced precipitation has been observed to cause positive phase changes as the particles precipitate in to the ionosphere at radiation belt L-shells (Clilverd et al., 2017).

In this section we illustrate how EMIC events are isolated with the LULU band-pass operator L_k^m (equation (7)). Band-pass filtered phase $z = L_k^m \phi$ (with $k = 5$, $m = 180$ min) of transmissions from NWC (Western Australia) to the receiver at SAN is analyzed. Increased phase is observed to coincide with IPDPs observed in Antarctic geomagnetic field observations. A number of EMIC events are identified in the X-component geomagnetic field at the Halley base in Antarctica during March–June 2016. Halley magnetometer data are used since there were no subsecond magnetometer data, needed to resolve the spectrum, available from SAN.

The series of panels in Figure 7 shows the spectrogram of B_X at Halley (top), overlaid with filtered phase z from NWC-SAN, and unprocessed amplitude and phase (bottom) for four active days and one quiet day in 2016. EMIC activity typically occurs between 18 and 22 UT on this path. The approximate phase change related to the apparent EMIC precipitation and substorm injections (discussed in the next subsection) are listed in Table 2.

Typical EMIC signatures in magnetic field spectrograms are characterized by the relatively brief (about 1–2 hr) periods of increased power at increasing frequencies within the Pc1-Pc2 band. These are seen near 20–21 UT (5 April 2016), 20:30–21:30 UT (13 May 2016), 22 UT (31 May 2016), and 19–20 UT (5 June 2016). On 31 May a transmitter shutdown causes the signal to drop out from about 12:00–15:00, causing large, random peaks in z until 16:00. Obviously, any peaks identified cannot be interpreted as anything physical and have not been plotted. The last panel is a quiet day for reference (1 March 2016).

The confirmed EMIC events all show a phase difference with $z > 90°$, coinciding with the IPDP in each case. Other potential EMIC events of $z > 50°$ are seen between 04 and 08 UT on 5 June 2016 and also between 14 and 15 UT on 5 April 2016. The increases in z appear to be associated with increased Pc1-Pc2 wave power, which are not clearly IPDP in form but may be associated with other types of Pc1-Pc2 waves appearing on the MLT morning or dayside. Maximum z on the quiet day (last panel of Figure 7), including daytime changes, is less than 40°.

4.3. Substorms

It has been shown that substorm-driven precipitation can be detected through their effects on narrow band transmissions (e.g., Beharrell et al., 2015; Clilverd et al., 2008). Clear substorm signatures are observed in Halley SCM B_X spectrum and z on 31 May 2016, depicted in the third panel of Figure 7. The band-pass filtered phase $z = L_k^m \phi$ (with $k = 5$, $m = 180$) shows the change in phase due to electron precipitation coincident with the substorm-induced unstructured broadband patches seen on the Halley SCM.

We see enhanced broad band activity at various times throughout the day, most notably the patches at approximately 07:30–10:15, 17:00–18:00, and 18:30–19:30. SuperMAG (Gjerloev, 2009) lists several substorm onset time on this day, with those observable on this path at 07:23, 15:37, and 18:36 UT. These events are strongly indicated by peaks in z starting to rise at about 07:40, 16:00, and 18:30. On this path MLT midnight occurs within about an hour of UT midnight.

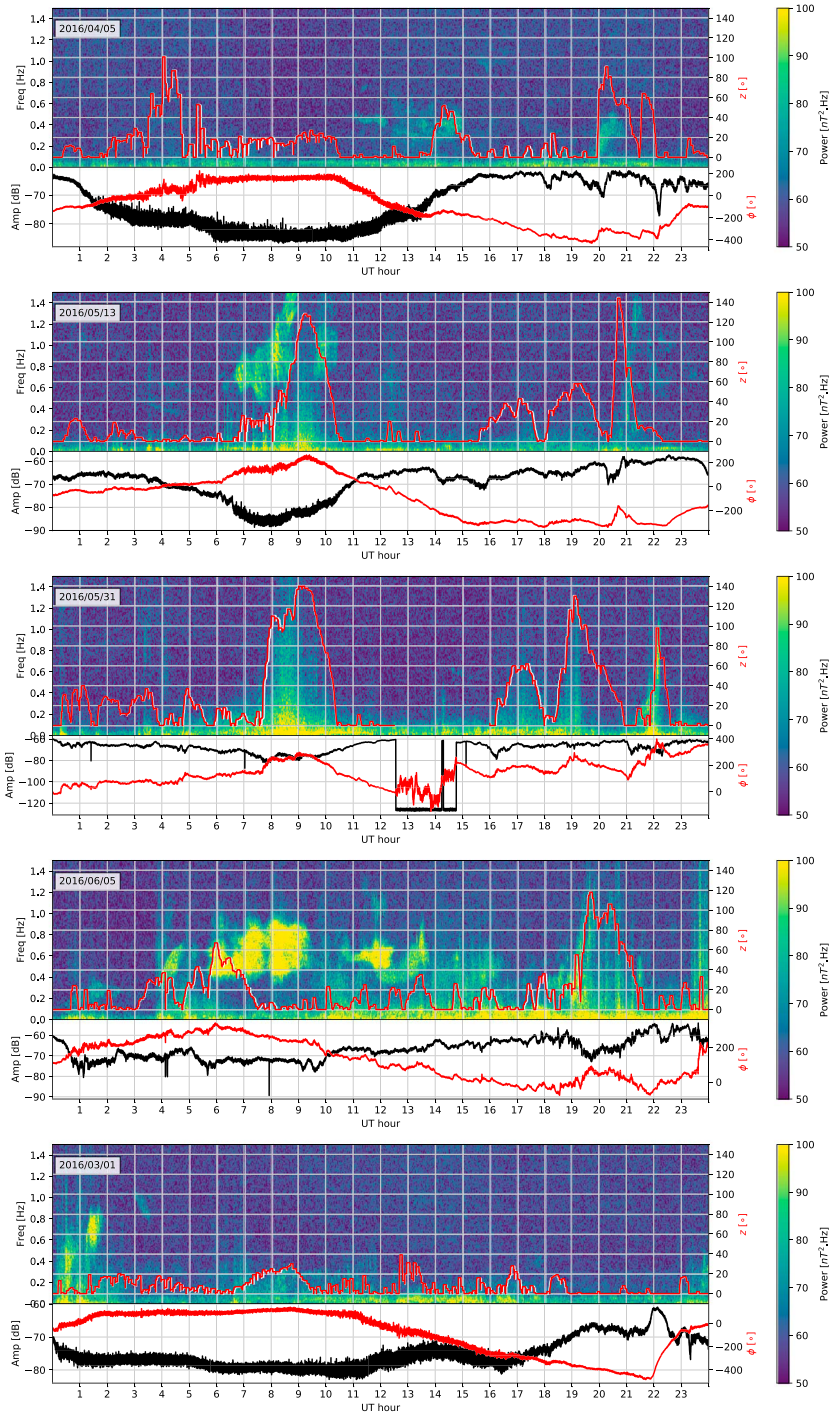

Figure 7. Magnetometer (B_X) spectrogram observed at Halley, with $z = L_k^m \phi$ (red) observed on the NWC-SAN propagation path over-plotted. In the lower part of every panel the original phase (red) and amplitude (black) is plotted for the same time interval. Each panel shows a day in 2016 when EMIC and/or substorm activity was observed, except the last panel, which illustrates a quiet day for reference.

Table 2
Start Time, End Time, and Phase Change Due to EMIC and SS Precipitation Events Observed on NWC-SAN Path

Date	Start	End	Max z (°)	Type
2016/04/05	20:00	21:00	92	EMIC
2016/05/13	20:30	21:45	161	EMIC
2016/05/13	08:00	10:30	128	SS
2016/05/31	21:15	22:15	115	EMIC
2016/05/31	07:40	10:20	140	SS
2016/05/31	18:30	20:50	130	SS
2016/06/05	18:45	20:00	100	EMIC

Note. SS = substorm; EMIC = electromagnetic ion cyclotron waves; NWC = North-West Cape; SAN = South African National Antarctic Expedition IV.

On 13 May (second panel of Figure 7) we see enhanced activity at broad band frequencies from about 06:30–10:30 UT in the B_X spectrum. The z parameter rises significantly at about 08:00 until 09:15, decreasing to the pre-event level at about 10:30 UT. This corresponds to the single SuperMAG-listed substorm event for this day with onset at 08:17 UT. Peaks z during substorm events are listed in Table 2, labeled "SS." All the events has $z > 120°$, while maximum quiet day z is less than 40°. This is suggestive of the utility of the L_k^m operator in identifying substorms, with appropriately chosen k and m. For example, substorms last longer than EMIC precipitation events, therefore peaks with wider support; therefore, lower and higher values of m could be used to distinguish between EMIC and substorm events.

5. Conclusions

Through the LULU operators an arbitrary signal can be decomposed in to blockpulses of specific widths, and the DPT enables the selection of a band of blockpulses. The band-pass operator (equation (7)) applied to a signal enables the selection of a specific range of resolution levels, which can easily be translated to physical phenomena. We showed examples how solar flares, substorms, and EMIC wave precipitation events are all relatively easily highlighted, based only on their typical duration.

It was shown that solar flares could be identified in narrow band phase data without the need to explicitly calculate and subtract a quiet day curve from the disturbed time series. The idempotence and variation preservation characteristics of the LULU operators enable clean extraction of relevant structures in the phase, which can be defined by setting typical duration times (e.g., between 5 and 200 min, used in section 4). Using the band-pass operator L_k^m does not replace the need for QDC removal completely, as phase can change rapidly near dawn and dusk, even on quiet days. The structure to be isolated should vary more rapidly than the typical diurnal variation of the signal. Additionally, more work is needed to accurately separate events occurring in rapid succession.

Setting resolution level and amplitude limits can enable the automatic detection of phenomena such as solar flares, which are critical to space weather monitoring services. Indeed, automatic flare detection was the initial inspiration for this work. A number of flares were detected automatically by setting a threshold of 40° for $z = L_k^m \phi$, with resolution levels set by $k = 5$ and $m = 200$ min during 6–10 September 2017. Some flares were weaker than would be expected; for example, the flare observed by GOES just before sunrise on 7 September had peak $z \approx 30°$. This suggests that this method, or at least the simple use of a 40° phase change threshold, is not adequate for flare identification outside of daytime hours. The correct identification of the daytime flare on 10 September shows the value of using (redundant) ground-based instrumentation for flare detection—This flare was correctly identified using our ground-based method while GOES observations were missing.

EMIC wave precipitation and substorm injections are readily detectable in phase using the band-pass operator L_k^m, set to only select positive pulses lasting from $k = 5$ to $m = 180$ min. Over the limited interval analyzed, both classes of events resulted in phase perturbations of at least 90°, while quiet days have $L_k^m \phi \lesssim 50°$. This suggests that a threshold-based selection may also be used to identify EMIC precipita-

tion and substorms. Night time events, however, are generally more difficult to detect since phase is more unstable after sunset than during day time.

In this paper the use of a class of nonlinear smoothers was demonstrated to be useful for detecting events that manifest in the *D* region ionosphere by smoothing or decomposing the phase of narrow band VLF signals that travel in the earth-ionosphere waveguide.

It was shown that these operators could be used to (i) isolate events based on duration, regardless of magnitude, and to (ii) isolate events without the explicit need for a quiet day curve.

The successful event detections presented in this paper suggests the potential for the LULU operators to be utilized for the automatic detection of various types of *D* region perturbations, without the need for potentially complex quiet day curving beforehand. Work continues on adapting the methods described in this paper to develop practical products for space weather monitoring.

Acknowledgments
This research was funded in part by a Newton International Exchanges grant (NI150103) from the Royal Society, United Kingdom. The data displayed in Figures 4 –7 may be downloaded from ftp://ftp.spacesci.sansa.org.za/pub/slotz/lotz_clilverd_201808/data/. We are grateful to Mark Engebreston and Mark Lessard for the long-term management of the search coil magnetometer at Halley base in Antarctica.

References

Anguelov, R., & Fabris-Rotelli, I. (2008). Discrete pulse transform of images. In A. Elmoataz, O. Lezoray, F. Nouboud, & D. Mammass (Eds.), *Image and Signal Processing* (pp. 1–9). Berlin Heidelberg: Springer.

Anguelov, R., & Fabris-Rotelli, I. (2010). LULU operators and discrete pulse transform for multidimensional arrays. *IEEE Transactions on Image Processing*, *19*(11), 3012–3023.

Beharrell, M., Honary, F., Rodger, C., & Clilverd, M. (2015). Substorm induced energetic electron precipitation: morphology and prediction. *Journal of Geophysical Research: Space Physics*, *120*, 2993–3008. https://doi.org/10.1002/2014JA020632

Carpenter, D. (1963). Whistler evidence of a "knee" in the magnetospheric ionization density profile. *Journal of Geophysical Research*, *68*, 1675–1682.

Clilverd, M. A., Duthie, R., Hardman, R., Hendry, A. T., Rodger, C. J., Raita, T., et al. (2015). Electron precipitation from EMIC waves: A case study from 31 May 2013. *Journal of Geophysical Research: Space Physics*, *120*, 3618–3631. https://doi.org/10.1002/2015JA021090

Clilverd, M. A., Rodger, C. J., Brundell, J., Ba, J., Cobbett, N., Moffat-Griffin, T., et al. (2008). Energetic electron precipitation during substorm injection events: High-latitude fluxes and an unexpected midlatitude signature. *Journal of Geophysical Research*, *113*, A10311. https://doi.org/10.1029/2008JA013220

Clilverd, M. A., Rodger, C. J., McCarthy, M., Millan, R., Blum, L. W., Cobbett, N., et al. (2017). Investigating energetic electron precipitation through combining ground-based and balloon observations. *Journal of Geophysical Research: Space Physics*, *122*, 534–546. https://doi.org/10.1002/2016JA022812

Clilverd, M. A., Rodger, C. J., Thomson, N. R., Brundell, J. B., Ulich, T., Cobbett, N., et al. (2009). Remote sensing space weather events: Antarctic-Arctic Radiation-belt (Dynamic) Deposition-VLF Atmospheric Research Konsortium network. *Space Weather*, *7*, S04001. https://doi.org/10.1029/2008SW000412

Cresswell-Moorcock, K., Rodger, C., Clilverd, M., & Milling, D. K. (2015). Techniques to determine the quiet day curve for a long period of subionospheric VLF observations. *Radio Science*, *50*, 453–468. https://doi.org/10.1002/2015RS005652

Gjerloev, J. W. (2009). A Global Ground-based magnetometer initiative. *Eos, Transactions American Geophysical Union*, *90*, 230–231. Retrieved from http://supermag.jhuapl.edu/substorms/

Hendry, A., Rodger, C., Clilverd, M., Engebretson, M., Mann, I., Lessard, M., et al. (2016). Confirmation of EMIC wave driven relativistic electron precipitation. *Journal of Geophysical Research: Space Physics*, *121*, 5366–5383. https://doi.org/10.1002/2015JA022224

Jankowitz, M. (2007). Some statistical aspects of LULU smoothers, University of Stellenbosch. Retrieved from http://scholar.sun.ac.za/handle/10019.1/1124

Rodger, C. J., Clilverd, M. A., Kavanagh, A. J., Watt, C. E. J., Verronen, P. T., & Raita, T. (2012). Contrasting the responses of three different ground-based instruments to energetic electron precipitation. *Radio Science*, *47*, RS2021. https://doi.org/10.1029/2011RS004971

Rodger, C. J., Raita, T., Clilverd, M. A., Seppälä, A., Dietrich, S., Thomson, N. R., & Ulich, T. (2008). Observations of relativistic electron precipitation from the radiation belts driven by EMIC Waves. *Geophysical Research Letters*, *35*, L16106. https://doi.org/10.1029/2008GL034804

Rohwer, C. H. (2005). *Nonlinear smoothers and multiresolution analysis*. Basel: Birkhäuser.

Thomson, N. R., Rodger, C. J., & Clilverd, M. A. (2005). Large solar flares and their ionospheric D region enhancements. *Journal of Geophysical Research*, *110*, A06306. https://doi.org/10.1029/2005JA011008

Wenzel, D., Jakowski, N., Berdermann, J., Mayer, C., Valladares, C., & Heber, B. (2016). Global ionospheric flare detection system (GIFDS). *Journal of Atmospheric and Solar-Terrestrial Physics*, *138-139*, 233–242.